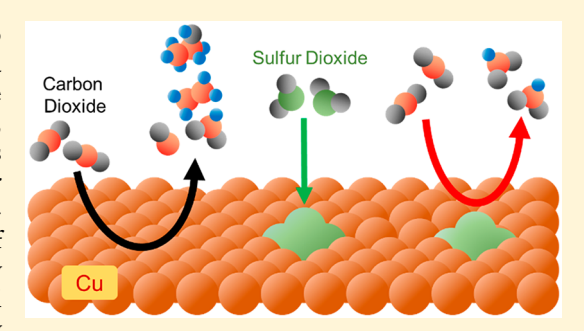


SO₂-Induced Selectivity Change in CO₂ Electroreduction

Wesley Luc,^{†,⊥} Byung Hee Ko,^{†,⊥} Shyam Kattel,[‡] Shuang Li,[§] Dong Su,^{§,} Jingguang G. Chen,*, and Feng Jiao*,^{†,}

Supporting Information

ABSTRACT: Electrochemical conversion of carbon dioxide (CO₂) to value-added chemicals has attracted much attention in recent years as a potential alternative to fossil resources. Although significant works have studied the influence of impurities in the electrolyte (e.g., metal ions), few studies have been performed to understand the influence of gaseous impurities in CO₂ electroreduction. Herein, we study the effects of sulfur dioxide (SO₂) on Ag-, Sn-, and Cu-catalyzed CO₂ electrolysis in a flowcell electrolyzer in near-neutral electrolyte, representing a broad range of CO₂ reduction catalysts. We show that the presence of SO₂ impurity reduces the efficiency of converting CO2 due to the preferential reduction of SO₂. In the cases of Ag and Sn, the effect of SO₂ impurity



was reversible and the catalytic activities of both catalysts were recovered. On the contrary, a shift in selectivity toward formate accompanied by a suppression of multicarbon (C_{2+}) products was observed on Cu catalyst, demonstrating that Cu is highly sensitive to SO₂ impurity. Our results suggest that CO₂ obtained from direct air capture technologies or biorefineries could be more suitable for Cu-catalyzed CO₂ electrolysis as these CO₂ sources would be relatively cleaner (SO₂-free) than fossil-derived sources such as power plants and can be directly coupled with distributed renewable energy sources such as wind and solar.

1. INTRODUCTION

The electrochemical production of value-added chemicals using carbon dioxide (CO₂) as the carbon source has attracted much attention in recent years and has been motivated by ever increasing CO₂ emission and anticipated cheap electricity prices derived from renewable energy sources. These efforts include fundamental investigation combining experimental and computational studies to establish design principles for the rational design of catalysts, 2 novel synthesis approaches for constructing high surface area materials with specified active sites,^{3,4} and reactor engineering to design practical devices.^{5–8} In the last case, the recent development of flow-cell electrolyzers, 8-10 in which catalysts are positioned on a wellengineered electrode-electrolyte interface allowing gaseous reactant to be fed from one side while electrolyte is fed on the other, has enabled the electrochemical conversion of CO2 at practical rates of reaction that cannot be achieved with typical batch reactors, further pushing this technology toward commercialization.

Critical to the development of CO₂ electrolysis technologies is also the key understanding of potential sources of impurities in the incoming feed (e.g., electrolyte and CO_2), as well as the identification of potential mechanisms for performance degradation. It has been well studied that trace impurities in the electrolyte such as metal ions (e.g., Fe²⁺ and Zn²⁺)¹¹ can

dramatically degrade CO₂ reduction performance where the catalytic surface can be irreversibly altered through the deposition of these metal ions under reducing potentials, shifting selectivities toward undesirable products.1 such as pre-electrolysis using sacrificial electrodes, 12 pretreatment of the electrolyte with metal-chelexing resin, 13 and designing catalysts where the catalytic surface can reconstruct under operating conditions¹⁴ have been proposed to overcome these challenges. Overall, the electrolyte most likely needs to be relatively pure and free of residual metal ions for commercial electrochemical conversion of CO₂. On the contrary, the effect of gaseous impurities in the CO2 feed has barely been studied, 15 and further work is necessary to elucidate the impact of such impurities on the performance in CO2 electrolysis.

The CO₂ feedstock for commercial CO₂ electrolysis can be obtained from direct air capture 16,17 or point sources such as power plants or chemical facilities. 18,19 The former is currently an area of intensive research due to the advantage of not being geographically limited; however, such technology has not yet been fully commercialized and still under pilot plant development. The latter accounts for a large fraction of

Received: March 25, 2019 Published: June 3, 2019

[†]Center for Catalytic Science and Technology, Department of Chemical and Biomolecular Engineering, University of Delaware, Newark, Delaware 19716, United States

^{*}Department of Physics, Florida A&M University, Tallahassee, Florida 32307, United States

[§]Center for Functional Nanomaterials, Brookhaven National Laboratory, Upton, New York 11973, United States

Department of Chemical Engineering, Columbia University, New York, New York 10027, United States

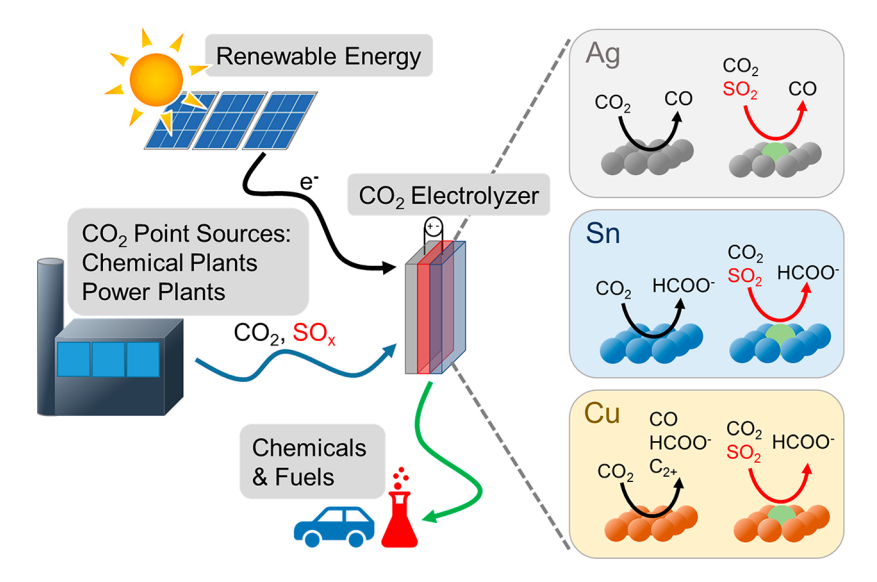


Figure 1. Schematic of CO₂ electrolyzer and potential feed sources.

anthropogenic CO₂ emissions with the current state-of-the-art CO₂ capture technology being amine-based absorption technologies. However, the exhaust streams from point sources such as power plants contain impurities such as SO_x, NO_x, or volatile organic compounds.²⁰ Although current carbon capture processes can purify these exhaust streams using energy intensive processes involving series of scrubbing and separating units, it is critical to understand how these impurities can affect CO₂ electrolysis to establish engineering criteria. To the best of our knowledge, the majority of CO₂ research to date uses highly pure CO₂ gas as reactant and little is known on the effect of gaseous impurities.

Herein, we study the influence of sulfur dioxide (SO₂) in the electrochemical conversion of CO2 in a flow-cell electrolyzer. Three different catalysts, silver (Ag), tin (Sn), and copper (Cu) as selective catalysts for producing carbon monoxide (CO), formate, and multicarbon (C_{2+}) products, respectively, are investigated as these materials are the most commonly studied in CO₂ electrolysis (Figure 1).¹¹ The catalysts are examined for CO2 reduction free of SO2 impurity, during the presence of SO₂, and finally after SO₂ exposure to determine if the gaseous impurity has an irreversible effect on the catalytic performance. The CO₂ reduction products are tracked over the course of electrolysis, and ex situ surface characterization is conducted at various time points during operation to elucidate the underpinning of catalytic change. The results show that the presence of SO₂ impurity in the incoming CO₂ feed reduces the efficiency of converting CO2 due to the preferential reduction of SO₂, as it is thermodynamically more favorable to reduce SO₂ than CO₂. In the cases of Ag and Sn catalysts, SO₂ impurity does not change the CO₂ reduction product selectivities and full recovery of the catalytic activities can be observed after the catalysts were exposed to SO₂. However, in the case of the Cu catalyst, SO₂ impurity has an irreversible, detrimental effect as the overall selectivity is shifted toward formate while suppressing the formation of C_{2+} products. Characterization and computational efforts indicate that the formation of copper(I) sulfide (Cu₂S) is likely responsible for the change in selectivity for Cu-catalyzed CO₂ electrolysis.

2. RESULTS AND DISCUSSION

Initial Characterization and Experimental Procedures. Commercial Ag, Sn, and Cu nanoparticles, representing a broad range of CO₂ reduction catalysts, were loaded on a gasdiffusion layer (GDL) with a catalyst loading of 0.3 mg cm⁻¹ using a drop-casting method as previously described.²¹ Scanning electron microscopy (SEM) images (Figure S1) show the well-dispersed nature of the nanoparticles on the GDL and the porosity of the catalyst layer, which is critical for maintaining the electrode-electrolyte interface by allowing facile transport of gaseous reactants and products to and away from the catalytic surface. Powder X-ray diffraction (PXRD) (Figure S2) of the as-purchased nanoparticles reveals the phase purity of the nanoparticles. In the cases of Sn and Cu nanoparticles, the presence of oxidized Sn and Cu in the form of SnO and Cu₂O, respectively, is apparent. The surface composition of the as-prepared electrodes was analyzed using ex situ X-ray photoelectron spectroscopy (XPS) (Figure S3). In the cases of Sn and Cu, the surfaces are partially oxidized, most likely from air exposure during sample handling. The asdeposited nanoparticles were analyzed for the influence of SO₂ on CO₂ electroreduction in a three compartment flow-cell electrolyzer (Figure S4) with two compartments for the anolyte and catholyte and one compartment for the gaseous reactants and products. Although previous studies have shown that conducting CO₂ electrolysis in alkaline electrolytes (e.g., KOH) has improvement in CO₂ reduction performance, 8, CO₂ strongly reacts with hydroxide (OH⁻) to form a bicarbonate/carbonate (KHCO₃⁻/CO₃²⁻) mixture, which degrades the electrolyte and reduces the efficiency of CO2 utilization. 9,23 Therefore, CO₂ electrolysis experiments were conducted in near-neutral conditions in 1.0 M potassium bicarbonate (KHCO₃) solution. A syringe pump was used to accurately control the feed rate of SO2 gas into the CO2 feed before entering the flow-cell electrolyzer, and electrolysis was conducted in the constant current mode. In short, pure CO₂ was initially fed for 30 min, then SO₂ was introduced into the CO₂ feed for 30 min, and then the SO₂ feed was stopped for the remainder of the electrolysis experiment. The gaseous products were quantified by an in-line gas-chromatography (GC) instrument during operation, while liquid products were Journal of the American Chemical Society

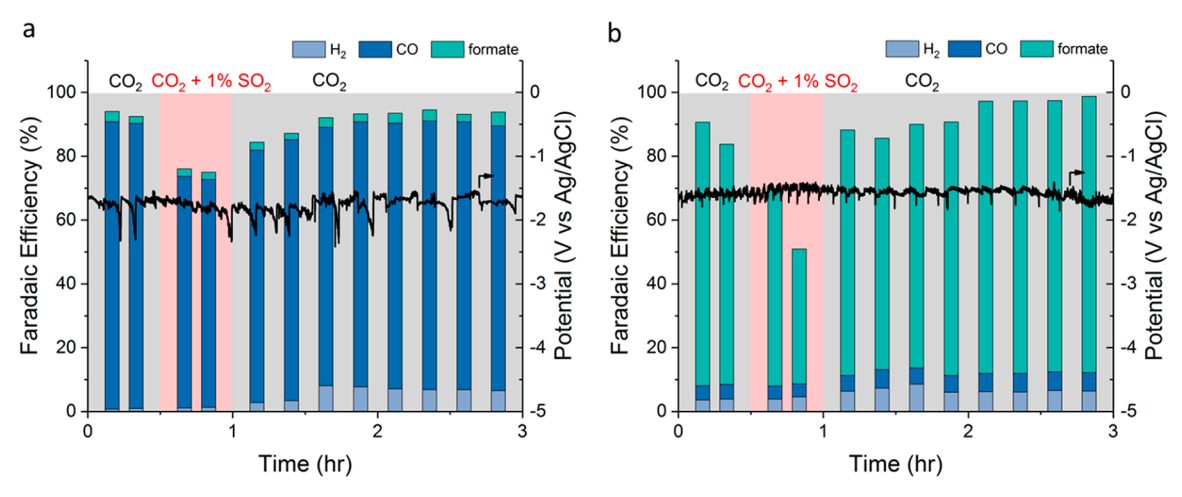


Figure 2. Performance of CO₂ + SO₂ electrolysis over (a) Ag and (b) Sn catalysts at constant current density of 100 mA cm⁻² in 1 M KHCO₃ over the span of 3 h. Corresponding Faradaic efficiencies can be found in Supporting Information (Tables S1 and 2).

collected and analyzed using nuclear magnetic resonance (NMR). Depending on the source, the concentration of SO₂ in flue gas is ~ 100 ppm ($\sim 0.01\%$); however, SO₂ concentration can be as high as ~10 000 ppm (~1%) in concentrated CO₂ streams that have not been desulfurized.²⁰ As a conservative limit, a stream of 1% SO₂ was chosen for initial studies.

Influence of SO₂ on Ag- and Sn-Catalyzed CO₂ **Electroreduction.** The influence of SO₂ on CO₂ (CO₂ + SO₂) electroreduction was first studied on Ag and Sn catalysts, as these materials are widely studied and commercial devices are currently being developed for the selective electrochemical conversion of CO₂ to CO and formic acid. 24,25 As shown in Figure 2, when pure CO₂ was initially fed, indeed high selectivities (>80%) toward CO and formate, respectively, were achieved on Ag and Sn catalysts in near-neutral electrolyte. The fluctuation in voltage is due to the accumulation of gas products as bubbles and eventual flush out of the catholyte chamber. However, when both catalysts were subjected to a stream of 1% SO₂ (Figure 2, red region), the total Faradaic efficiencies toward CO2 reduction products decreased, and the remaining charge balance is likely attributed to the reduction of SO₂ since it is thermodynamically more favorable to reduce SO_2 than CO_2 (e.g., $SO_2 + 4H^+ + 4e^- \rightarrow S$ $+ 2H_2O, E^{\circ} = 0.50 \text{ V}; CO_2 + 2H^{+} + 2e^{-} \rightarrow CO + H_2O, E^{\circ} =$ $-0.11 \text{ V; } \text{CO}_2 + 2\text{H}^+ + 2\text{e}^- \rightarrow \text{HCOOH, } E^\circ = -0.25 \text{ V}).$ There is also a large overpotential to drive SO₂ reduction under CO2 electrolysis conditions. Previous ultrahigh vacuum studies have also indicated the facile adsorption of SO2 on transition metal surfaces and in most cases, catalyzed-activation of SO₂ near room temperature. 26,27 To further elucidate the adsorption of SO₂ compared to CO₂, Gibbs free energy of adsorption as well as binding energies were calculated (Table S3), and calculations indeed show that SO₂ adsorption is stronger on all surfaces (Ag, Sn, and Cu) compared to that of CO₂. This further suggests the preferential reduction of SO₂ over CO₂. XPS measurements confirmed the reduction of SO₂ toward the formation of metal sulfide species (Figures S5 and 6, Table S4), and XPS measurements at each time point were obtained from separate electrolysis experiments with new electrodes operating for different durations. On the basis of the peak positions at 161.7 and 161.6 eV, the metal sulfides were identified as Ag₂S and SnS₂ with surface concentrations of \sim 35.6 atom % and \sim 3.3 atom % on Ag and Sn catalysts, respectively. ^{28–30} Sulfite (SO₃^{2–}) and sulfate (SO₄^{2–}) were also detected. The former is likely formed during sample handling from residual surface metal oxides reacting with SO₂ in the presence of water when no potential is applied, and the latter is likely formed from the natural oxidation of metal sulfides.³¹ The observed shifts in Ag peak position to lower binding energies are likely due to the presence of S species, since Ag has a lower electronegativity than S (S, 2.59; Ag, 1.87). 32,33 On the contrary, the shifts in Sn peak position are due to different concentrations of tin oxides (SnO/SnO₂) in each sample as Sn rapidly oxidizes in air during sample handling. Due to the resolution of the spectrometer, accurately differentiating these two oxides is difficult. The formation of surface metal sulfides (Ag₂S and SnS₂) was also confirmed with high angle annular dark field scanning transmission electron microscopy (HAADF-STEM) and electron energy loss spectrum (EELS) imaging (Figures S7 and S8), which shows S species positioned near the edges of the particles. Bright field (BF) transmission electron microscopy (TEM) imaging and the corresponding selected area electron diffraction (SAED) indeed show the formation of SnS₂ (Figure S8f). In the case of Ag (Figure S7f), diffraction patterns associated with Ag₂S were not observed, indicating that the structure of Ag₂S is likely amorphous. This observation was further confirmed with high resolution (HR)-TEM (Figure S9), showing an amorphous layer on the surface of the Ag catalyst. For all TEM work, FAA ionomer binder was used instead of Nafion, as Nafion has sulfonic functional groups that would convolute the detection of S species associated with the metal sulfides. SEM images (Figures S10 and S11), after 1 h of electrolysis with both catalysts subjected to a feed of 1% SO₂ for 30 min, show the formation of bulky particles with smooth surfaces, a common characteristic of metal sulfides. Future work using density functional theory (DFT) can provide additional insight on the mechanism of metal sulfide formation during CO₂ electrolysis. It must be noted that the exact surface characteristic under reaction condition remains unclear due to the lack of in situ surface sensitive methods and the limitation of ex situ measurements. Gas chromatography-mass spectrometry (GC-MS) was also employed to detect other possible sulfur-containing species; however, the only sulfur-containing species detected was unreacted SO2. It is likely that other residual species were produced below the detection limit and cannot be easily detected by GC-MS or NMR.

Journal of the American Chemical Society

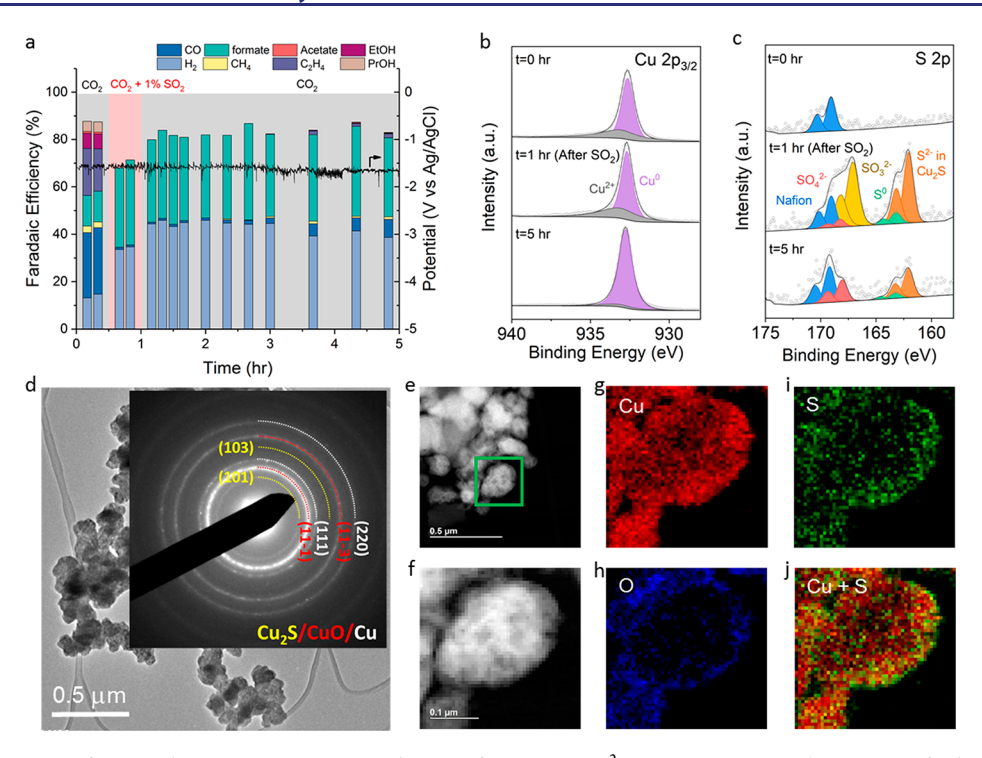


Figure 3. (a) Performance of Cu catalyst at constant current density of 100 mA cm⁻² in 1 M KHCO₃ with a 1% SO₂ feed over the span of 5 h. Corresponding Faradaic efficiencies can be found in Supporting Information (Table S5). XPS spectrum of (b) Cu and (c) S region at various time points. (d) BF-TEM image. Inset: SAED pattern, (e, f) HAADF-STEM images, and (g-j) EELS mapping of Cu catalyst after 1 h of electrolysis in CO₂ + SO₂ experiment, subjected to a 1% SO₂ feed for 30 min.

Interestingly, when the feed of SO₂ was stopped, the CO₂ reduction performance recovered on both catalysts, and in the case of Sn, a slight improvement in formate Faradaic efficiency was observed. A recent study has suggested that doping Sn surfaces with sulfur (S) atoms and then selectively removing S atoms can create highly active undercoordinated Sn sites for improved CO₂ reduction to formate.³⁰ Thermodynamically, Ag₂S and SnS₂ are not stable under CO₂ electrolysis conditions, and this was confirmed with postreaction XPS that shows a decrease in metal sulfides (Table S4). Particle aggregation can be seen in postreaction SEM images, which is likely due to surface rearrangement from the reduction of metal sulfides (Figures S10 and S11). The SO₂ + CO₂ experiments suggest that the presence of small amounts of metal sulfides (Ag₂S and SnS₂) on Ag and Sn catalysts does not shift the CO2 reduction product selectivities, as the dominant CO₂ reduction products remained as CO and formate, respectively. However, the reduction of the total CO2 reduction Faradaic efficiency indicates that SO₂ impurity can reduce the efficiency of converting CO₂, since the reduction of SO₂ is more favorable than CO₂. Sn catalyst was also examined under longer SO₂ exposure (Figure S12), and a plateauing of total Faradaic efficiency was observed (~50%), suggesting a steady-state competitive reaction between SO2 and CO2 reduction. To further understand the effect of SO₂ near flue gas concentrations, both Ag and Sn catalysts were subjected to 0.01% SO₂ (Figure S13), and the results show that SO₂ at lower concentration does not significantly affect CO2 electroreduction performance for both catalysts.

Influence of SO_2 on Cu-Catalyzed CO_2 Electroreduction. Next, $CO_2 + SO_2$ electroreduction experiments were performed on Cu catalyst to study the influence of SO_2 on Cu-catalyzed CO_2 reduction, as Cu is the only

monometallic material that can reduce CO2 to high-value C₂₊ products with appreciable selectivities. As shown in Figure 3a, indeed Cu can convert CO₂ to an array of products including CO, formate, ethylene (C2H4), ethanol (EtOH), npropanol (PrOH), and a small amount of acetate and methane (CH₄). Long-term CO₂ electrolysis over Cu catalyst demonstrates a stable performance of converting CO₂ to C₂₊ products (Figure S14). When the Cu catalyst was subjected to 1% SO₂ (Figure 3a, red region), as similar to both Ag and Sn catalysts, the total CO2 reduction Faradaic efficiency decreased, likely due to preferential reduction of SO₂. Interestingly, the CO₂ reduction product selectivity shifted, and formate became the dominant CO₂ reduction product, while the other CO₂ reduction products were suppressed. XPS analysis (Figure 3b and Figure 3c) shows the formation of metal sulfide (Table S4) after 1 h of electrolysis, and the peak position at ~162.0 eV was assigned to Cu₂S with a surface concentration of ~12 atom %. 34 This peak assignment was also verified with commercial Cu₂S and copper(II) sulfide (CuS) particles (Figure S15). Again, sulfite and sulfate were also detected likely due to sample handling. Unreacted SO2 was the only sulfur-containing compound that was detected with GC-MS; however, there is likely residual compounds produced under the detection limit. The formation of aggregated bulkylike particles after 1 h of electrolysis, subjected to a feed of 1% SO₂ for 30 min, can be seen (Figure S16), and this observation was further confirmed with BF-TEM imaging (Figure 3d). The corresponding SAED pattern shows the presence of residual Cu₂S, metallic Cu, and CuO that was likely formed from air exposure during sample handling. Similar to the Ag and Sn catalysts, HAADF-STEM and the corresponding EELS imaging (Figure 3e-j) reveal highly dispersed S species positioned near the edges of the particles, suggesting that Cu₂S

likely resides near the surface. This observation was also confirmed with HR-TEM imaging and the corresponding fast Fourier transform (FTT) pattern (Figure S17), also showing the formation of Cu₂S near the particle surface. Additional HAADF-STEM and EELS mapping can be found in the Supporting Information (Figure S18). Again, FAA ionomer binder was used instead of Nafion for TEM work. On the asprepared Cu catalyst, there were no S species detected (Figure S19). The utilization of FAA ionomer showed a similar trend in CO₂ + SO₂ electroreduction as Nafion and thus the ionomer is likely not the cause of the observed shift in selectivity (Figure S20). Again, the exact surface characteristic under reaction condition remains unclear due to the lack of in situ surface sensitive methods to examine Cu particles at high current densities in CO2 electrolysis. However, Chorkendorff, Jaramillo, and co-workers very recently demonstrated that the surface structure of polycrystalline Cu thin film is fully converted to the metallic phase under CO electroreduction conditions by using in situ grazing incident X-ray diffraction with a synchrotron radiation source.³⁵ Future work employing similar techniques could further elucidate the surface structure of Cu in the presence of SO₂ under CO₂ electrolysis conditions, and this may provide additional insight on the formation of surface Cu₂S.

When the SO₂ feed was stopped, formate remained as the dominant CO2 reduction product, and an incremental recovery was observed as the selectivity toward CO production slowly increased, followed by C₂H₄ production. Mechanistically, this observation is consistent with literature as it is well-known that the pathway toward C2+ products goes through a CO intermediate on Cu-catalyzed CO2 electroreduction, while the pathway toward formate is a dead end.³⁶ Therefore, the observed trend in recovery is CO followed by C₂₊ products. In addition, an enhancement in hydrogen evolution was also observed during and after SO₂ exposure. Similar to Ag₂S and SnS₂, Cu₂S is also thermodynamically unstable under CO₂ electrolysis conditions. However, even after 5 h of electrolysis, Cu₂S was still detected on the Cu surface (Figures 3c and S21), indicating that the reduction of Cu₂S is kinetically slow. The presence of Cu₂S may be the reason for the inability of the Cu catalyst to recover its initial performance, and the observation in the current study is consistent with previous works that have shown that S-modified nanostructured Cu catalysts can selectively convert CO₂ to formate.^{37,38} In addition, commercial Cu₂S particles were also examined and the dominant CO₂ reduction product was formate (Figure S22), further supporting that surface Cu₂S is likely responsible for the change in selectivity.

To further probe the sensitivity of the Cu catalyst toward SO_2 impurity, similar experiments were conducted with lower SO_2 concentrations (0.1% and 0.01%). In both cases, a shift in selectivity toward formate was observed (Figures S23 and S24), and XPS measurements confirmed the presence of Cu_2S (Table S6). With lower SO_2 concentrations, there was a relatively faster rate of recovery; however full recovery was not achieved even after 5 h of electrolysis. Again, an incremental recovery of CO followed by C_{2+} products can be seen. A recovery up to ~10% and ~5% for CO and C_2H_4 Faradaic efficiencies, respectively, was achieved in 0.1% SO_2 after 5 h. At lower concentration of 0.01% SO_2 , the recovery of CO and C_2H_4 quickly plateaued to those same Faradaic efficiencies, and no further improvement was observed. Postreaction XPS analysis after 5 h electrolysis shows similar Cu_2S composition

on both catalytic surfaces after 0.1% and 0.01% SO_2 treatments (Table S6), suggesting that there may be residual surface Cu_2S that are stable under CO_2 electrolysis conditions. In an attempt to recover the initial performance after 1% SO_2 , the flow-cell electrolyzer was operated at 1 A cm⁻² for 30 min under Ar to locally generate a high-flux of hydrogen to potentially reduce the metal sulfides (Figure S25). Although slight improvements were observed, a full recovery was not achieved, and postreaction XPS analysis also indicated the presence of Cu_2S (Table S6). These observations suggest that Cu catalysts are sensitive to SO_2 and that residual Cu_2S on the catalytic surface may dramatically impact the CO_2 electroreduction performance. Therefore, it is concluded that the CO_2 gas feed must be relatively pure $(SO_2$ -free) for Cu-catalyzed CO_2 electrolysis.

Density Functional Theory Calculations. To further gain insight on the shift in selectivity, DFT calculations were performed on S modified Ag, Sn, and Cu catalysts, and the surfaces were modeled as S-doped Ag(111), Sn(111), and Cu(111), respectively. The binding energies of the hydrogen evolution reaction intermediate (e.g., *H) and CO₂ reduction intermediates for CO production (e.g., *COOH) and formate production (e.g., *OCHO) were calculated on clean and S-doped surfaces (Table S7). The DFT optimized geometries on Cu(111) and S-doped Cu(111) (Figure 4) show that *H

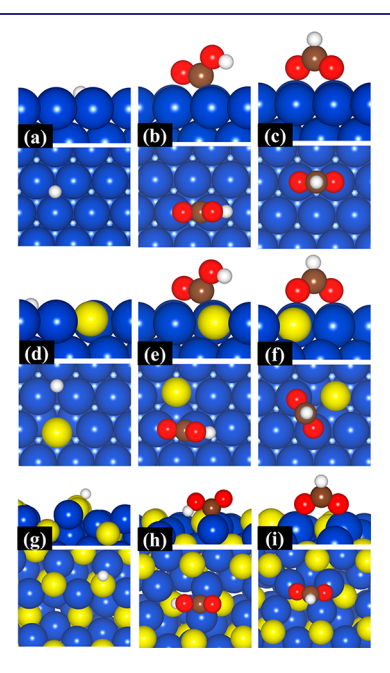


Figure 4. DFT optimized binding configurations of (a) *H, (b) *COOH, and (c) *OCHO on Cu(111), (d) *H, (e) *COOH, and (f) *OCHO on S-doped Cu(111), and (g) *H, (h) *COOH, and (i) *OCHO on $Cu_2S(100)$. Blue: Cu. Yellow: S. Red: O. Brown: C. White: H.

prefers to bind at a hollow site; *COOH binds at a top site via C atom, and *OCHO binds at top sites via two O atoms. The binding geometries of these intermediates on undoped and S-doped (111) surfaces of Ag and Sn were also found to be similar to those on Cu(111). It is noted that *OCHO is relatively more stable than the *COOH intermediate on all surfaces, and the stability of *OCHO increases in the order Sn(111) > Ag(111) > Cu(111).

The binding energies (Table S7) show that *OCHO is more stable than *COOH by 1.25, 1.35, and 1.13 eV on Ag(111), Sn(111), and Cu(111), respectively. In contrast, the *OCHO stability over *COOH (0.62 eV) decreases on S-doped Ag(111) compared to Ag(111). However, the *OCHO stability over *COOH increases on S-doped Sn(111) (1.54 eV) and S-doped Cu(111) (1.23 eV) compared to Sn(111) and Cu(111), respectively. To account for the formation of Cu₂S as experimentally observed, further DFT calculations were performed to calculate binding energies of *H, *COOH, and *OCHO (Figure 4) on the Cu₂S(100) surface that has mixed Cu and S surface termination. Consistent with the prediction on S-doped Cu(111), the results show that the *OCHO stability over *COOH (1.24 eV; Table S7) is enhanced on Cu₂S(100) compared to Cu(111). In summary, the DFT calculations predict that surface S atoms on Cu surfaces selectively stabilize *OCHO, and thus the formation of formate is promoted, in agreement with the experimental observations. A similar promotional effect on the formate selectivity is predicted on S-doped Sn (111). However, such promotion is not predicted on S-doped Ag(111) since the *OCHO stability over *COOH is less on S-doped Ag(111) than on Ag(111). It must be noted that there is a discrepancy between experimental and computational predication on the Ag catalyst as DFT predicts that formate is more favorable than CO formation, while experimentally, CO was observed as the major CO₂ reduction product. A similar discrepancy is also highlighted in a recent work by Smith and co-workers.³⁹ However, by incorporating solvation effects on transition states and surface coverage of *H, *COOH, and *OCHO, they successfully demonstrated the promotion of CO over formate formation on the Ag surface. Future work should also focus on exploring these effects on Sn- and Cu-catalyzed CO₂ reduction.

3. CONCLUSIONS AND OUTLOOK

In summary, the influence of SO_2 impurity on Ag-, Sn-, and Cu-catalyzed CO_2 electrolysis was studied in a flow-cell electrolyzer. The results show that the presence of SO_2 impurity reduces the efficiency of converting CO_2 as the reduction of SO_2 is thermodynamically more favorable. In the cases of Ag and Sn, full recovery was observed after both catalysts were subjected to SO_2 and the selectivities of converting CO_2 to CO and formate were preserved, respectively. However, in the case of Cu, the catalytic performance was highly sensitive to SO_2 and a shift in selectivity toward formate, accompanied by a suppression of C_{2+} products, was observed. Computational efforts suggest that residual Cu_2S formed on the surface, as confirmed with XPS characterization, is likely responsible for the shift in selectivity.

Our experimental observations further motivate the development of direct air capture (DAC) technologies as the CO₂ feedstock from these sources would be relatively cleaner than that obtained from fossil-burning point sources such as power plants and chemical facilities. The main challenge is the capture and concentration of CO₂ from a dilute source, the air. Although DAC technologies has yet been fully commercialized and previous cost estimation has indicated that these technologies are too expensive (>\$600 per ton of CO₂) to be practical,⁴⁰ small pilot-plant facilities, such as the Climeworks AG facility in Switzerland with the ability to capture 900 tons of CO₂ annually,⁴¹ are currently being developed. A recent work by Keith and co-workers has provided the first comprehensive cost breakdown of a DAC facility, estimating

the cost to be between \$94 and \$232 per ton of ${\rm CO_2}$. Another advantage of DAC is that it is not geographically limited, and thus, this technology can be coupled with distributed renewable energy sources that is expected to be inexpensive in the near future. 1

Lastly, additional work should also focus on studying the influence of NO_x as well as O₂ impurities in CO₂/CO electrolysis. Although the concentration of NO, and O2 may be trace amount in the CO₂ feed, these impurities may also have detrimental effect on CO₂/CO electrolysis as demonstrated by the current SO₂ study. Similarly, both NO₃ and O₂ could coadsorb on the catalytic sites under reducing potentials or interact with the electrolyte, potentially altering the local environment or surface structure and consequently influencing catalytic performance. In particular, it has been hypothesized that subsurface oxygen atoms in Cu-catalyzed CO₂/CO electroreduction may potentially enhance the formation of C_{2+} products, 42 and it would be interesting to determine if adsorbed oxygen species can influence the catalytic performance. Thus, future work should focus on further understanding the influence of these gaseous impurities on CO₂/CO electroreduction activity.

4. EXPERIMENTAL SETUP

Electrode Preparation. Commercial Ag (<100 nm, 99.5%) and Cu (25 nm) powders were purchased from Sigma-Aldrich. Commercial Sn (0.1 μ m), IrO₂ (99.99%), Cu₂S (99.5%), and CuS (99.8%) powders were purchased from Alfa Aesar. The catalyst inks were prepared by mixing 25 mg of metal particles, 20 μ L of Nafion solution (5 wt % in 50/50 water and isopropanol), and 3 mL of isopropanol. After the catalyst inks were sonicated for at least 30 min prior to drop casting, 0.3 mg cm⁻² of the metal particles were drop casted onto a Sigracet 29 BC GDL (Fuel Cell Store). Ag, Sn, and Cu electrodes were used as anodes.

CO₂ Electrolysis in Flow-Cell Electrolyzer. The electrochemical measurements were conducted in a three chamber flow-cell electrolyzer with channel dimensions of 2 cm \times 0.5 cm \times 0.15 cm. 1 M KHCO₃ (99.95%, Sigma-Aldrich) was fed to the catholyte and anolyte chamber at \sim 1 mL min⁻¹ with peristaltic pumps. CO₂ was fed to the flow-cell at 17 sccm via a Brooks GF40 mass flow controller, while SO₂ was fed from a syringe via a syringe pump (Cole-Parmer) at 0.17, 0.017, and 0.0017 sccm. To obtain SO₂ gas, a H-cell was continuously purged with SO₂ (Matheson Gas) for 30 min and then a 10 mL gastight syringe (no. 1010, Hamilton Company) was used to extract the gas. The cathode and anode chambers were separated by a FAA-3 hydroxide exchange membrane (Fumatech). The backpressure of the gas in the gas chamber was controlled via a backpressure controller (Cole-Parmer).

Chronopotentiometry experiments were conducted via an Autolab PG128N. The half-cell potentials were measured using an external Ag/AgCl reference electrode (Pine Research). The resistance between the cathode and reference electrode was determined using the current-interrupt technique prior to electrolysis, and the measured applied potential was iR-corrected after electrolysis. The gas products were sampled directly to a multiple gas analyzer no. 5 gas chromatography system (SRI Instruments) equipped with a Molsieve 5A and a HayeSep D column connected to a thermal conductivity detector (TCD) and a flame ionization detector (FID). The electrolytes containing liquid products were collected at the exit of the flow cell for 200 s and were analyzed using ¹H NMR with water suppression using a presaturation method (Bruker AVIII 600 MHz NMR spectrometer). 500 μ L of collected sample was mixed with 100 μL of D₂O containing 25 ppm (v/v) dimethyl sulfoxide (99.9%, Alfa Aesar) as the internal standard. To prevent SO₂ from entering the GC during SO_2 injection, a base trap was positioned between the outlet of the flow-cell electrolyzer gas chamber and the inlet of the GC. Ar was

fed at 15 sccm through a tee-connector to push the gas products along with unreacted CO_2 through the base trap before entering the GC for quantification. In order to detect potential sulfur-containing products, the outlet gas stream from the electrolyzer was connected to a gastight batch cell and was continuously purged. A gastight syringe (Hamilton Company) was used to draw and inject the gas sample into an integrated GC–MS (Aglient 59771A) system equipped with a DB-FFAP column and a mass spectrometry system. The mass fragmentation patterns were compared to those of the National Institute of Standards and Technology (NIST) database. As for the catalyst recovery, a National Instruments power source (RMX-4121) was used to achieve a current density of 1 A cm $^{-2}$. After 30 min of electrolysis under Ar, the flow-cell electrolyzer was disassembled, the cathode was quickly dried due to severe flooding, and new anode was replaced prior to CO_2 electrolysis.

Material Characterization. PXRD was conducted using Cu K α radiation source (Bruker D8 Discover diffractometer). SEM images were obtained from Auriga 60 CrossBeam. XPS was performed with a K-Alpha X-ray photoelectron spectrometer system (Thermo Fisher Scientific). All peaks were fitted with Thermo Avantage software with the C 1s signal calibrated to 284.8 eV.

For TEM characterization, the samples were thoroughly washed with DI water immediately after reaction to remove the residual electrolyte and then gently abraded from the GDL support to acquire particles for the TEM experiment. In order to distinguish the sulfur atoms that correspond to Cu₂S, FAA ionomer binder was used instead of Nafion binder, since Nafion has sulfonic functional groups. Bright field (BF), high-resolution transmission electron microscopy (HRTEM) images and selected area electron diffraction pattern (SAED) were performed with a transmission electron microscope (JEM-2100F, JEOL) at an acceleration voltage of 200 kV. High angle annular dark field scanning transmission electron microscopy (HAADF-STEM) images and electron energy loss spectrum (EELS) were obtained on a Hitachi HD2700C STEM with a probe aberration corrector.

Computational Methods. Spin polarized periodic density functional theory (DFT) 43,44 calculations were performed at the GGA level within the PAW-PW91 formalism 45,46 using the Vienna Ab Initio Simulation Package (VASP) code. 47,48 The total energy calculations were performed using a 3 \times 3 \times 1 Monkhorst–Pack grid 49 and a plane wave cutoff energy of 400 eV.

Cu(111), Ag(111), and Sn(111) surfaces were modeled using a four layer 3×3 surface slab. One surface Cu, Ag, and Sn atom was replaced with a S atom to model S-doped Cu(111), Ag(111), and Sn(111) surfaces, respectively. A vacuum layer of ~15 Å thick was added in the slab cell along the direction perpendicular to the surface to minimize the artificial interactions between the surface and its periodic images. During geometry optimization, atoms in the bottom two layers were fixed and all other atoms including adsorbates were allowed to relax until the force on each ion was smaller than 0.02 eV/Å. The binding energy (BE) of an adsorbate was calculated as

$$\mathrm{BE}_{(\mathrm{adsorbate})} = E_{(\mathrm{slab} + \mathrm{adsorbate})} - E_{(\mathrm{slab})} - E_{(\mathrm{adsorbate})}$$

where $E_{({\rm slab+adsorbate})}$, $E_{({\rm slab})}$, and $E_{({\rm adsorbate})}$ are the total energy of slab with adsorbate, the energy of clean slab, and the energy of adsorbate in the gas phase, respectively. $E({\rm H})$ is taken as one-half the total energy of the ${\rm H_2}$ molecule during the calculation of hydrogen binding energy.

The free energy of adsorption of SO_2 and CO_2 on Cu(111), Ag(111), and Sn(111) at T=298.15 K was calculated as

$$\Delta G_{\rm ad} = G_{\rm (slab+adsorbate)} - G_{\rm (slab)} - G_{\rm (adsorbate)}$$

where $G = E(\mathrm{DFT}) + \mathrm{ZPE} - T\Delta S$. $E(\mathrm{DFT})$ is the total energy obtained from DFT calculations, and ZPE and $T\Delta S$ are zero point energy and entropic contributions, respectively. The DFT calculations were performed to calculate ZPE of adsorbed species. ZPE and $T\Delta S$ values of gas phase species were taken from NIST database.

ASSOCIATED CONTENT

S Supporting Information

The Supporting Information is available free of charge on the ACS Publications website at DOI: 10.1021/jacs.9b03215.

Schematic of flow-cell electrolyzer, SEM and TEM images, XPS analysis, tables of Faradaic efficiencies, and theoretical calculations (PDF)

AUTHOR INFORMATION

Corresponding Authors

*J.G.C.: jgchen@columbia.edu *F.J.: jiao@udel.edu

ORCID ®

Dong Su: 0000-0002-1921-6683 Feng Jiao: 0000-0002-3335-3203

Author Contributions

¹W.L. and B.H.K. contributed equally to this work.

Notes

The authors declare no competing financial interest.

ACKNOWLEDGMENTS

This material is based upon work supported by the Department of Energy under Award DE-FE0029868. The authors at the University of Delaware also thank the National Science Foundation for financial support (Award CBET-1803200). DFT calculations were supported by the U.S. Department of Energy, Catalysis Program (Grant DE-FG02-13ER16381). This research used resources of the Center for Functional Nanomaterials, which is a U.S. DOE Office of Science Facility, at Brookhaven National Laboratory under Contract DE-SC0012704.

REFERENCES

- (1) Haegel, N. M.; Margolis, R.; Buonassisi, T.; Feldman, D.; Froitzheim, A.; Garabedian, R.; Green, M.; Glunz, S.; Henning, H. M.; Holder, B.; Kaizuka, I.; Kroposki, B.; Matsubara, K.; Niki, S.; Sakurai, K.; Schindler, R. A.; Tumas, W.; Weber, E. R.; Wilson, G.; Woodhouse, M.; Kurtz, S. *Science* 2017, 356, 141.
- (2) Seh, Z. W.; Kibsgaard, J.; Dickens, C. F.; Chorkendorff, I. B.; Norskov, J. K.; Jaramillo, T. F. Science 2017, 355, eaad4998.
- (3) Lu, Q.; Rosen, J.; Zhou, Y.; Hutchings, G. S.; Kimmel, Y. C.; Chen, J. G. G.; Jiao, F. *Nat. Commun.* **2014**, *5*, 3242.
- (4) Rosen, J.; Hutchings, G. S.; Lu, Q.; Forest, R. V.; Moore, A.; Jiao, F. ACS Catal. 2015, 5, 4586.
- (5) Ripatti, D. S.; Veltman, T. R.; Kanan, M. W. Joule 2019, 3, 240.
- (6) Delacourt, C.; Ridgway, P. L.; Kerr, J. B.; Newman, J. J. Electrochem. Soc. 2008, 155, B42.
- (7) Kim, B.; Hillman, F.; Ariyoshi, M.; Fujikawa, S.; Kenis, P. J. A. *J. Power Sources* **2016**, 312, 192.
- (8) Verma, S.; Lu, X.; Ma, S. C.; Masel, R. I.; Kenis, P. J. A. Phys. Chem. Chem. Phys. **2016**, 18, 7075.
- (9) Verma, S.; Hamasaki, Y.; Kim, C.; Huang, W. X.; Lu, S.; Jhong, H. R. M.; Gewirth, A. A.; Fujigaya, T.; Nakashima, N.; Kenis, P. J. A. ACS Energy Letters 2018, 3, 193.
- (10) Ma, S. C.; Sadakiyo, M.; Luo, R.; Heima, M.; Yamauchi, M.; Kenis, P. J. A. J. Power Sources **2016**, 301, 219.
- (11) Hori, Y.; Wakebe, H.; Tsukamoto, T.; Koga, O. Electrochim. Acta 1994, 39, 1833.
- (12) Hori, Y.; Konishi, H.; Futamura, T.; Murata, A.; Koga, O.; Sakurai, H.; Oguma, K. Electrochim. Acta 2005, 50, 5354.
- (13) Wuttig, A.; Surendranath, Y. ACS Catal. 2015, 5, 4479.
- (14) Weng, Z.; Zhang, X.; Wu, Y. S.; Huo, S. J.; Jiang, J. B.; Liu, W.; He, G. J.; Liang, Y. Y.; Wang, H. L. Angew. Chem., Int. Ed. 2017, 56, 13135.

- (15) Zhai, Y. M.; Chiachiarelli, L.; Sridhar, N. ECS Trans. 2009, 19, 1.
- (16) Sanz-Perez, E. S.; Murdock, C. R.; Didas, S. A.; Jones, C. W. Chem. Rev. 2016, 116, 11840.
- (17) Keith, D. W.; Holmes, G.; St. Angelo, D.; Heidel, K. *Joule* **2018**, 2, 1573.
- (18) Koytsoumpa, E. I.; Bergins, C.; Kakaras, E. J. Supercrit. Fluids 2018, 132, 3.
- (19) Wu, X. M.; Yu, Y. S.; Qin, Z.; Zhang, Z. X. 12th International Conference on Greenhouse Gas Control Technologies 2014, GHGT-12; Dixon, T., Herzog, H., Twinning, S., Eds.; Energy Procedia, Vol. 63; Curran, 2015; p 1339.
- (20) Last, G. V.; Schmick, M. T. Identification and Selection of Major Carbon Dioxide Stream Compositions; Pacific Nortwest National Laboratory: Richland, WA, 2011.
- (21) Lv, J. J.; Jouny, M.; Luc, W.; Zhu, W. L.; Zhu, J. J.; Jiao, F. Adv. Mater. 2018, 30, 1803111.
- (22) Dinh, C. T.; Burdyny, T.; Kibria, M. G.; Seifitokaldani, A.; Gabardo, C. M.; de Arquer, F. P. G.; Kiani, A.; Edwards, J. P.; De Luna, P.; Bushuyev, O. S.; Zou, C. Q.; Quintero-Bermudez, R.; Pang, Y. J.; Sinton, D.; Sargent, E. H. Science 2018, 360, 783.
- (23) Dinh, C. T.; de Arquer, F. P. G.; Sinton, D.; Sargent, E. H. ACS Energy Lett. 2018, 3, 2835.
- (24) Liu, Z. C.; Yang, H. Z.; Kutz, R.; Masel, R. I. J. Electrochem. Soc. 2018, 165, J3371.
- (25) Yang, H. Z.; Kaczur, J. J.; Sajjad, S. D.; Masel, R. I. ECS Trans. 2017, 77, 1425.
- (26) Haase, J. J. Phys.: Condens. Matter 1997, 9, 3647.
- (27) Rodriguez, J. A.; Jirsak, T.; Chaturvedi, S.; Hrbek, J. J. Am. Chem. Soc. 1998, 120, 11149.
- (28) Ghafoor, S.; Ata, S.; Mahmood, N.; Arshad, S. N. Sci. Rep. **2017**, 7, 255.
- (29) Hota, G.; Idage, S. B.; Khilar, K. C. Colloids Surf., A 2007, 293, 5.
- (30) Zheng, X. L.; De Luna, P.; de Arquer, F. P. G.; Zhang, B.; Becknell, N.; Ross, M. B.; Li, Y. F.; Banis, M. N.; Li, Y. Z.; Liu, M.; Voznyy, O.; Dinh, C. T.; Zhuang, T. T.; Stadler, P.; Cui, Y.; Du, X. W.; Yang, P. D.; Sargent, E. H. Joule 2017, 1, 794.
- (31) Aastrup, T.; Wadsak, M.; Leygraf, C.; Schreiner, M. J. Electrochem. Soc. 2000, 147, 2543.
- (32) Mann, J. B.; Meek, T. L.; Knight, E. T.; Capitani, J. F.; Allen, L. C. J. Am. Chem. Soc. **2000**, 122, 5132.
- (33) Allen, L. C. J. Am. Chem. Soc. 1989, 111, 9003.
- (34) Xie, Y.; Riedinger, A.; Prato, M.; Casu, A.; Genovese, A.; Guardia, P.; Sottini, S.; Sangregorio, C.; Miszta, K.; Ghosh, S.; Pellegrino, T.; Manna, L. J. Am. Chem. Soc. 2013, 135, 17630.
- (35) Scott, S. B.; Hogg, T. V.; Landers, A. T.; Maagaard, T.; Bertheussen, E.; Lin, J. C.; Davis, R. C.; Beeman, J. W.; Higgins, D.; Drisdell, W. S.; Hahn, C.; Mehta, A.; Seger, B.; Jaramillo, T. F.; Chorkendorff, I. Acs Energy Letters 2019, 4, 803.
- (36) Ren, D.; Fong, J. H.; Yeo, B. S. Nat. Commun. 2018, 9, 925.
- (37) Shinagawa, T.; Larrazabal, G. O.; Martin, A. J.; Krumeich, F.; Perez-Ramirez, J. ACS Catal. 2018, 8, 837.
- (38) Deng, Y. L.; Huang, Y.; Ren, D.; Handoko, A. D.; Seh, Z. W.; Hirunsit, P.; Yeo, B. S. ACS Appl. Mater. Interfaces 2018, 10, 28572.
- (39) Bohra, D.; Ledezma-Yanez, I.; Li, G. N.; de Jong, W.; Pidko, E. A.; Smith, W. A. Angew. Chem., Int. Ed. 2019, 58, 1345.
- (40) Lackner, K. S.; Brennan, S.; Matter, J. M.; Park, A. H. A.; Wright, A.; van der Zwaan, B. *Proc. Natl. Acad. Sci. U. S. A.* **2012**, *109*, 13156.
- (41) www.climeworks.com.
- (42) Eilert, A.; Cavalca, F.; Roberts, F. S.; Osterwalder, J.; Liu, C.; Favaro, M.; Crumlin, E. J.; Ogasawara, H.; Friebel, D.; Pettersson, L. G. M.; Nilsson, A. J. Phys. Chem. Lett. 2017, 8, 285.
- (43) Hohenberg, P.; Kohn, W. Phys. Rev. 1964, 136, B864.
- (44) Kohn, W.; Sham, L. J. Phys. Rev. 1965, 140, A1133.
- (45) Blochl, P. E. Phys. Rev. B: Condens. Matter Mater. Phys. 1994, 50, 17953.

- (46) Perdew, J. P.; Wang, Y. Phys. Rev. B: Condens. Matter Mater. Phys. 1992, 45, 13244.
- (47) Kresse, G.; Furthmuller, J. Comput. Mater. Sci. 1996, 6, 15.
- (48) Kresse, G.; Hafner, J. Phys. Rev. B: Condens. Matter Mater. Phys. 1993, 48, 13115.
- (49) Monkhorst, H. J.; Pack, J. D. Phys. Rev. B 1976, 13, 5188.